

Investigating the Influence of Residual Stresses on Fatigue Crack Growth for Additively Manufactured Titanium Alloy Ti6Al4V by using Peridynamics

Olena Karpenko*, Selda Oterkus, Erkan Oterkus

Department of Naval Architecture, Ocean and Marine Engineering, University of Strathclyde, 100 Montrose Street, Glasgow G4 0LZ, United Kingdom

*Corresponding author: olena.karpenko@strath.ac.uk

Keywords: Peridynamics; Additive manufacturing; residual stresses; fatigue performance prediction

Abstract

This study presents a numerical approach to predict the influence of the residual stresses on Fatigue Crack Growth Rates (FCGR). The main focus is on the additively manufactured titanium alloy Ti6Al4V with resultant high residual stresses in the samples due to the layer by layer manufacturing. A parabolic temperature profile has been applied to represent the effect of the pre-tension or pre-compression of the sample to account for the existence of the initial residual stresses. The proposed approach has been validated using experimental data available in the literature showing the capability of the tool to predict the FCGR.

1 Introduction

Additive manufacturing (AM) process becomes a state-of-the-art manufacturing technology of complex shaped metal parts [1]. The great potential of AM is due to productivity, reputability, and geometrical flexibility. The structures can be manufactured from a variety of materials, including stainless steel, titanium, nickel-based alloys, aluminium [2,3], which are used in different fields based on their mechanical properties.

The fabrication process is based on the layer by layer adding of material according to the designed 3D geometry [4]. Thus, the AM process provides a lot of advantages over the

conventional processing methods such as prototyping, rapid fabrication, product customisation and material efficiency. On the other hand, the layer-wise production resulting in material anisotropy, process-induced defects and residual stress development. It is recognised that the disadvantages of AM exist due to the high impact on the mechanical behaviour of the final product with properties worse than the conventionally produced components [5–7]. The variations in the microstructure occur due to the high-temperature gradients, which are moving to the rapid solidification during the AM. Moreover, thermal gradients produce residual stresses in the sample, and while the solidification of the layer mainly introduces the shrinkage of the sample, the ‘printing’ of the additional layer can change the residual stresses from tensile to compressive and the other way around. The process of the rapid and repeated heating and cooling of layer by layer manufacturing is also resulting in variations of the residual stresses where the stresses are larger in the scanning direction [8]. These quantities generally influence the fatigue performance of the material.

Several studies are performed on the properties of the material of additively manufactured parts, analysing the effects of AM processing conditions and the ways of improving the final product quality [9,10]. Thijs et al. [11] studied the influence of the scanning parameters and scanning strategies of Selective Laser Melting (SLM) AM on microstructure and pore initiations. Leuders et al. [8] applied heat-treatment and Hot Isostatic Pressing (HIP) techniques to improve the fatigue strength of SLM produced samples. The as-built samples showed very high tensile internal stresses with the highest residual stresses in the scanning direction, which strongly influenced FCGR. The post-built annealing treatments almost eliminated the residual stresses and reduced microstructure anisotropy leading to fatigue performance close to the wrought sample. The HIP process reduced the size of the pores in the samples and showed a very high impact on fatigue life, where the crack initiated at the process-induced defects. Vrancken et al. [12] also reported anisotropy in FCGR of Ti6Al4V produced by SLM, where very high compressive stresses influenced the FCGR originated along with the building directions. On the other hand, the samples with dominated tensile residual stresses showed the

lowest fracture toughness. Multiple studies [13,14] on the material outcome of the AM process showcased the residual stress distributions in the as-built samples with high compressive stresses at the centre of the samples and tension at the edges. Syed et al. [14] also investigated the influence of the residual stresses on FCGR and observed high dependency of residual stresses on fatigue crack growth behaviour. Moreover, it was showcased that the orientation of the sample cut had a different outcome of FCGR with higher residual stresses resulting in a higher FCGR. All of the studies on Ti6Al4V samples produced by SLM observed the largest residual stresses parallel to the scan direction, and the studies [12–14] outlined the importance of post-built annealing treatments to relieve the residual stresses and reduce the anisotropy of mechanical properties.

Despite multiple experimental studies performed to understand the mechanisms for the residual stress generation in SLM, several numerical studies were conducted to estimate the residual stresses and distortions in the samples. Mughal et al. [15] developed a 2D finite element thermo-mechanical model with moving heat source to predict the residual stresses. Moreover, Alimardani et al. [16] proposed a 3D transient approach for layer by layer modelling and predicting the temperature redistributions and residual stresses in the multi-layered samples. Mukherjee et al. [17] performed 3D thermo-mechanical models and evaluated the effect of the AM process parameters such as layer thickness and heat input on the residual stress distributions. Another study [18] also coupled 3D thermo-mechanical FE models and additionally analysed residual stress distributions due to the different laser scan strategies.

The studies in the literature showcased two types of Compact Tension (C(T)) sample production by AM for the fatigue crack growth tests. The first type of specimens by SLM was built individually on the platform, and the second type involved the building of the continuous extended block, which later on is used to slice individual specimens [12]. Each of the produced samples was then machined to have the smooth sample surface according to ASTM standard E647 [19] and after the notch was produced. Looking at the production process of C(T) samples, Syed et al. [14] showed the changes in the residual stresses with the applied surface

and notch machining. Firstly, the as-built individual samples had very high compressive stresses in the middle of the sample and as twice as high tensile stresses at the sample edges. Secondly, after machining of the sample surfaces, the sample became slightly thinner and the compressive stresses in the middle were released by 55% with some release to the tensile stresses at the edges of the sample. Moreover, the last machining of the notch resulted not only in the tensile stress reduction but also in the stress redistribution. The machining process had a noticeable effect on the stress release in the samples, but stresses still varied, with tensile and compressive stresses within the sample length.

On the other hand, the heat treatment resulted in almost neglectable stresses in the samples or quite low constant stresses through the sample length. The fatigue tests of the SLM C(T) samples showed faster crack propagation with higher residual stresses. A similar outcome in the fatigue propagation tests was showcased by other authors [8,12] indicating the effect of anisotropy in the fatigue properties of the samples due to the higher residual stress in the build direction compared to the layer scanning direction. In each of the studies, the resultant residual stresses have huge variations with some as-built samples having very high tensile residual stresses of up to 800 MPa [8,12,14], up to 300 MPa [8,17,20] and some with very high compressive stresses of up to -400 MPa [12–14,21].

This study aims to analyse the effect of residual stresses in the C(T) specimens on FCGR by means of Peridynamics (PD). The numerical PD fatigue model is developed to predict the fatigue performance of wrought titanium alloy and after introducing the internal stresses in the model by different temperature profiles. Thus, the FCGR are analysed and compared to the test data available in the literature. Finally, the studies about the residual stresses formed in the AM samples as a consequence of the repeated heating and cooling processes are reviewed. The developed PD model with the thermal stress implementation will illustrate the great impact on the FCGR. The presented numerical results in the Fatigue Crack Growth (FCG) studies are verified with Finite Element Analysis (FEA).

2 Method

The numerical model used in the current study is based on bond-based PD [22], including PD's extension for fatigue damage predictions [23]. A detailed overview of the numerical method is introduced in [24], where the authors applied PD numerical modelling and analysis on fatigue crack nucleation problems. The current studies' numerical model is extended to FCG problems and applied to AM structures with initial residual stresses.

In general, in the bond-based PD model, the body is discretised with material points \mathbf{x} , where each of the points interacts with each other and physical interaction is referred to as 'bond'. The PD equation of motion in Eq. (1) governs the motion of the material points, and the interaction between the points is represented by pairwise force densities $\mathbf{f}_{(i)(j)}$ and is given by Eq. (2) [25].

$$\rho_{(i)} \ddot{\mathbf{u}}_{(i)} = \sum_{j=1}^{N_{FM}} \mathbf{f}_{(i)(j)} V_{(j)} \psi(\mathbf{x}_{(j)} - \mathbf{x}_{(i)}, N) + \mathbf{b}_{(i)} \quad (1)$$

$\rho_{(i)}$, $\ddot{\mathbf{u}}_{(i)}$ and $\mathbf{b}_{(i)}$ are the mass density, acceleration and body load of the material point i , respectively. N_{FM} is the total number of material points (family members) within the horizon of the material point i . $V_{(j)}$ is the volume of the material point j . ψ is a function that represents the broken bonds between material points.

$$f_{(i)(j)} = c(s_{(i)(j)} - \alpha T_{(i)(j)}) \frac{\mathbf{y}_{(j)} - \mathbf{y}_{(i)}}{|\mathbf{y}_{(j)} - \mathbf{y}_{(i)}|} \quad (2)$$

where \mathbf{y} is the deformed position of a material point, c is the micromodulus and $s_{(i)(j)}$ is the stretch of the bond between material points. The body in the current study is also subjected to a temperature change T with the coefficient of thermal expansion α , where $T_{(i)(j)} = 0.5(T_{(j)} + T_{(i)})$.

PD micromodulus c is calibrated by matching the elastic strain energy density of classical continuum mechanics to the PD strain energy density of a material point inside a body subjected to simple loading conditions [26]. Due to the type of the samples used for the fatigue

analysis with the thick samples loaded in a single plane, a 2-Dimensional model with plane strain assumptions is used, and micromodulus is expressed in terms of Young's modulus, E , thickness, h , and horizon size, δ :

$$c = \frac{48E}{5\pi h\delta^3} \quad (3)$$

The relative elongation of the bonds is defined as ‘stretch’, and when the stretch $s_{(i)(j)}$ reaches a given limit value s_c , the bond between the points i and j breaks irreversibly.

Due to the nature of the cycling loading with the two load extremes of P_{min} and P_{max} , the PD fatigue model includes the minimum s^{min} and maximum s^{max} bond stretches between material points, which define the cyclic bond strain $\varepsilon = |s^{max} - s^{min}|$.

According to [23], the cyclic bond strain ε is proportional to the cyclic Stress Intensity Factor (SIF), which leads to the relationship between the PD FCG parameters and the Paris law. Well known Paris’ law is reported as:

$$\frac{da}{dN} = C\Delta K^M \quad (4)$$

where C and M are the constants determined from the experiments, and ΔK is SIF range. And with the correlation of ΔK to the ε , Eq. (4) can be rewritten as:

$$\begin{cases} \frac{d\lambda(N)}{dN} = -A_1\varepsilon^{m_1} \text{ (Phase I)} \\ \frac{d\lambda(N)}{dN} = -A_2\varepsilon^{m_2} \text{ (Phase II)} \end{cases} \quad (5)$$

where $\lambda(N)$ is the damage variable called the “remaining life”. $\lambda(N)$ is applied on each bond of the material’s points interactions and degrades under the increased number of cycles N . With the initial remaining life of $\lambda(0) = 1$ for an intact bond, the bond is breaking irreversibly due to fatigue when $\lambda(N) \leq 0$.

To take into account the damage initiation due to fatigue, the failure parameter introduced in [27], which includes a history-dependent scalar-valued function ψ to represent broken interactions (bonds) between material points, is included in the PD equation of motion in Eq. (1). The function ψ depends on λ in the following way:

$$\psi(\mathbf{x}_{(j)} - \mathbf{x}_{(i)}, N) = \begin{cases} 1 & \text{if } \lambda(N) > 0 \text{ for all } 1 < N \\ 0 & \text{otherwise} \end{cases} \quad (6)$$

The presented numerical fatigue model in Eq. (5) includes two phases of fatigue, where PD fatigue parameters A_1, m_1 are for crack nucleation (Phase I) and A_2, m_2 are for crack propagation (Phase II). The fatigue parameters for both phases are calibrated with the experimental data, where the calibration of A_1, m_1 for Phase I is explained in [24]. For Phase II, the cyclic bond strain ε is proportional to the cyclic SIF [23] and the PD fatigue parameters are calibrated by matching $\frac{da}{dN} - \Delta K$ curves with experimental data, where PD parameter $m_2 = M$ can be obtained directly from the Paris' law data. Moreover, the parameter A_2 has to be calibrated, where the single PD FCG simulation is performed with an arbitrary value of A_2' and already calibrated value of m_2 . After evaluation of the PD FCGR $\left(\frac{da}{dN}\right)'$ with the estimated value of A_2' and because the FCGR linearly depends on A_2 , the calibrated value of A_2 can be computed in the following way [23]:

$$A_2 = A_2' \frac{da/dN}{(da/dN)'} = A_2' \frac{C \Delta K^M}{(da/dN)'} \quad (7)$$

If the sample has already a pre-existing crack, then the PD FCG model has both phases, and the material points located in the vicinity of the crack tip are treated as in Phase II.

3 Validation of PD Fatigue model

The PD study of the fatigue performance is conducted for the C(T) samples, where the main interest is in the FCG resistance due to the tensile-tensile loading conditions. The wrought titanium alloy Ti6Al4V with the following homogeneous material properties is selected: Young's modulus $E = 110 \text{ GPa}$ and Poisson's ratio $\nu = 1/3$.

In the PD fatigue model described in Section 2 two phases are included in the current study: crack nucleation and propagation phases. The C(T) sample is discretised with the material points and the points located in the vicinity of the crack tip are already in the crack propagation phase, and as the crack propagates the points in front of the crack tip will be

switching from nucleation to propagation phase. For each of the phases, the PD parameters A and m should be identified. First of all, the PD parameters A_1 and m_1 are calibrated from the experimental data [28] and then A_2 and m_2 are obtained from the Paris' law data [29].

For the crack nucleation phase, a dog-bone plate in Fig. 1a with the total length of $L = 50 \times 10^{-3}m$, width of $W = 20 \times 10^{-3}m$ and $W_{in} = 6 \times 10^{-3}m$, thickness of $h = 4 \times 10^{-3}m$ is selected. The PD model in Fig. 1b is discretised with 6600 material points with uniform spacing between them $\Delta x = 0.3 \times 10^{-3}m$ and horizon size of $\delta = 3.015\Delta x$.

The dog-bone plate is under high cycle fatigue with the load ratio of $R = 0.1$ and the stress amplitudes of $\sigma_a = 373, 322, 297$ and $244MPa$ are applied as body force densities b_y in the PD model [26]. The calibration process described in [23] is performed using S-N test data [28], shown in Fig. 2, which resulted in $A_1 = 1 \times 10^4$ and $m_1 = 4.42$, with the fatigue life predictions within the range of test data [28] as shown in Fig. 3.

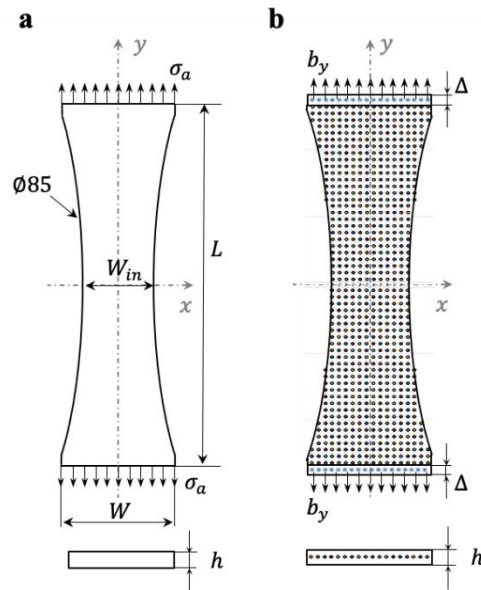


Fig. 1 a Dog-bone plate dimensions and **b** PD model discretisation.

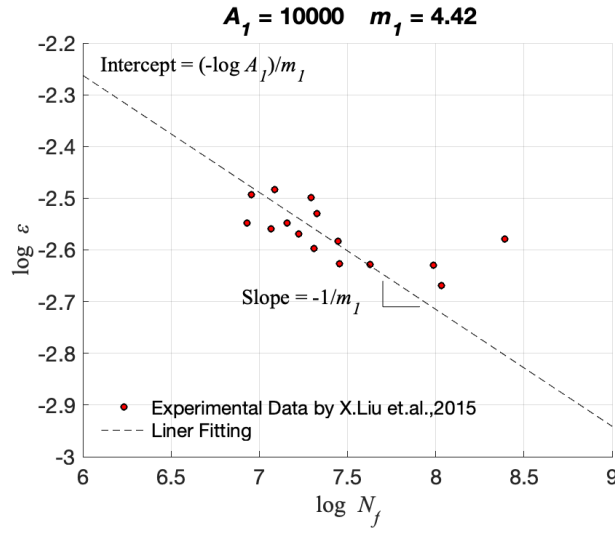


Fig. 2 Loading cycles N_f as a function of bond strain ε for the crack nucleation phase.

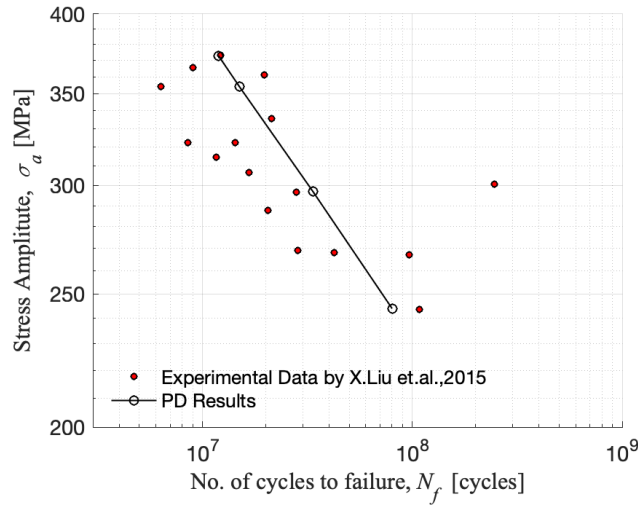


Fig. 3 Stress amplitude as a function of the loading cycle.

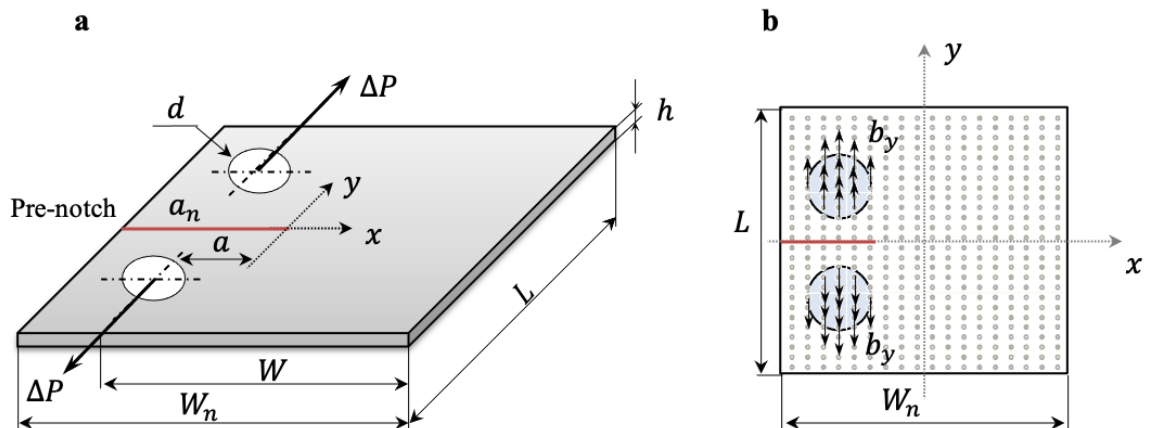


Fig. 4 a Square titanium alloy C(T) plate under uniaxial tensile loading and **b** its PD model discretisation.

For the crack propagation phase, the PD parameters A_2 and m_2 are obtained from the Paris' law data [29] and the simulations are performed for the C(T) sample as shown in Fig. 4. The

following dimensions are considered: width of $W_n = 30 \times 10^{-3}m$, length of $L = 31.25 \times 10^{-3} m$, thickness of $h = 5 \times 10^{-3}m$ and the length of pre-notch is $a_n = 12.4 \times 10^{-3}m$. The sample is under cyclic load of $\Delta P = 3.15 kN$ with the load ratio of $R = 0.1$, which are applied on the pins with the diameter of $d = 6.25 \times 10^{-3}m$ as a body force density [26] in the following form:

$$b_y = \frac{P_y}{\Delta V_\Delta} \quad (8)$$

where ΔV_Δ is the volume of the pin area, and P_y is the applied tension/compression load, which is defined as:

$$P_y = \begin{cases} P_y^{max} = \frac{2\Delta P}{1-R} \\ P_y^{min} = P_y^{max}R \end{cases} \quad (9)$$

where P_y^{max} and P_y^{min} are the cyclic load extremes.

PD model of C(T) sample is discretised with 10400 material points with uniform spacing between them $\Delta x = 0.3 \times 10^{-3} m$ and horizon size of $\delta = 3.015\Delta x$. The calibration of the parameters $A_2 = 0.52 \times 10^6$ and $m_2 = 4.757$ is obtained using Paris law data [29], where the SIF is obtained from ASTM standard E647 [19]:

$$\Delta K = \frac{\Delta P(2 + \zeta)}{h\sqrt{W}(1 - \zeta)^{\frac{3}{2}}} (0.886 + 4.64\zeta - 13.32\zeta^2 + 14.72\zeta^3 - 5.6\zeta^4) \quad (10)$$

where $\zeta = \frac{a}{W}$, a is crack length from the location of the applied load, h is the thickness of the specimen, and W is the distance between the applied load and the edge of the specimen.

The numerical results of FCGR in Fig. 5 are presented by the Paris curves, where fracture toughness is evaluated by Eq. (10) when $\zeta > 0.2$. The fatigue crack growth behaviour with the calibrated PD parameters is in good agreement with the experimental data [29]. The following PD model performed for the wrought Ti6Al4V is used as a reference model for studies presented in the next sections.

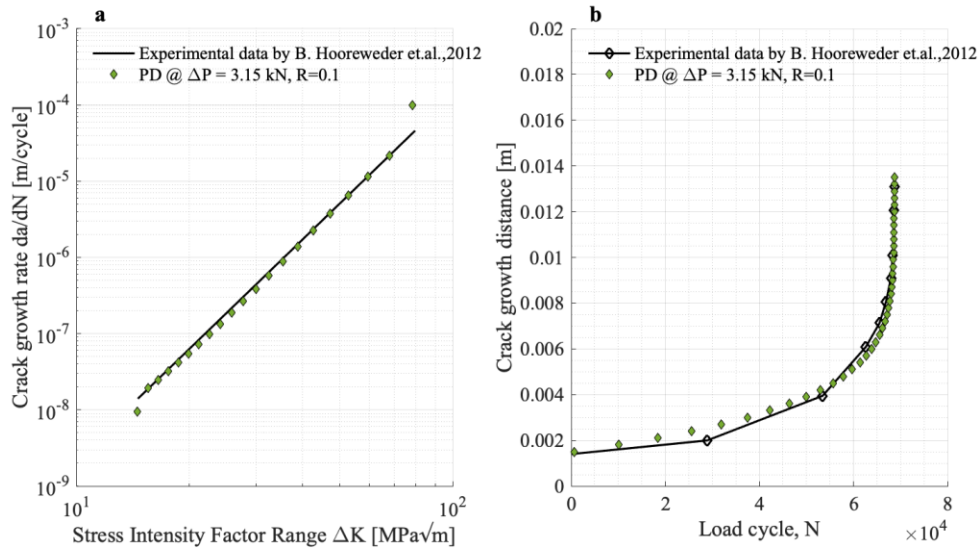


Fig. 5 a Crack growth rate versus SIF range and **b** Crack growth distance versus load cycle.

4 Influence of the residual stresses on the fatigue crack growth

The PD fatigue model consists of multiple static tension-compression cycles. Due to this, the implementation of the residual stresses was simplified and a pre-tension or pre-compression model due to thermal deformation is introduced. Moreover, the applied temperature distributions are the same in each cycle and the residual stresses will be readjusted due to the crack propagation only. In this study, the model is treated as elastic and the residual stresses are compressive in both x and y directions or tensile in both directions.

Firstly, the FEA analysis of the thermally deformed structure is performed using the commercial software ANSYS to identify the residual thermal stresses due to the heat source. Secondly, FEA is used to evaluate the maximum residual stress in the C(T) sample under different temperature distributions, and PD numerical model is verified with FEA. Lastly, the fatigue crack propagation analysis by means of PD is performed on titanium alloy C(T) sample with initial stresses due to the applied temperature profile.

4.1 FEA of residual stresses in C(T) specimen

FEA is conducted to evaluate the residual stresses in the C(T) specimen. In general, the AM process resulting in very high residual stresses due to repeated heating and layered cooling process. The stresses depend on the temperature distributions, especially when the produced

deposit cools down. The residual stresses tend to change from compressive to tensile in the middle of the samples and from tensile to compressive between the layers, with a non-uniform distribution of residual stresses within the sample [17]. In order to introduce the residual stresses in titanium alloy C(T) specimen, the temperature boundary conditions should be specified. Fig. 6 shows the configured temperature distribution. Please note that the selected paraboloid temperature distribution does not represent the real temperatures in the additively manufactured C(T) samples but is selected by the iterative procedure to reach the specific levels of residual stresses in the numerical sample. Four types of parabolic temperature distributions are selected with $T_{\max} = -250, 250, 500$ and 1000 K with the resulting residual stresses shown in Fig. 7.

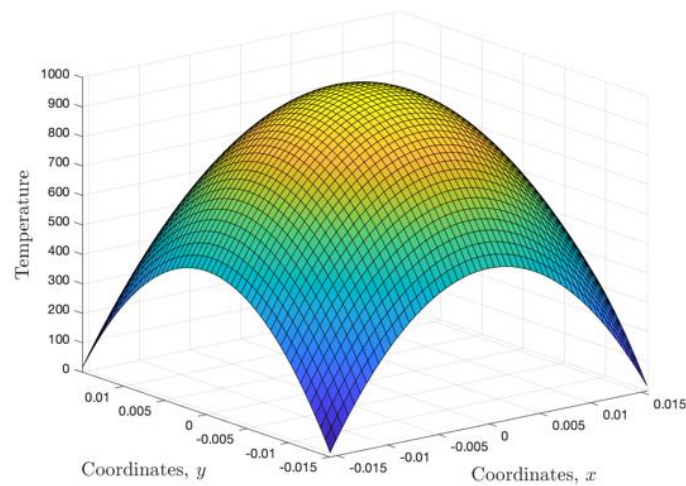


Fig. 6 Parabolic temperature distributions in C(T) sample with $a = 0$ under $T_{\max} = 1000\text{ K}$

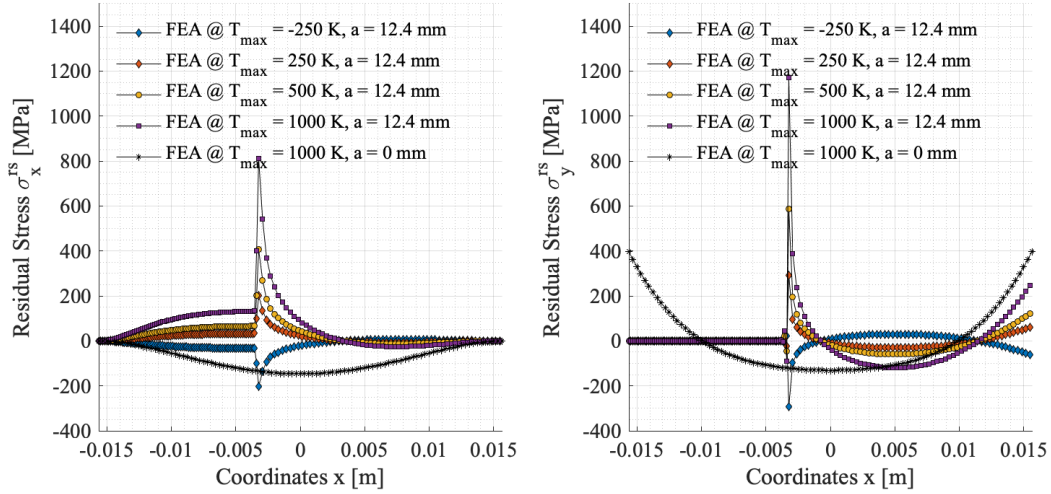


Fig. 7 Residual stress distribution in the C(T) sample along the centre line $y = 0$ for a crack length of $a = 0$ and $a = 12.4 \text{ mm}$ due to the different temperature profiles

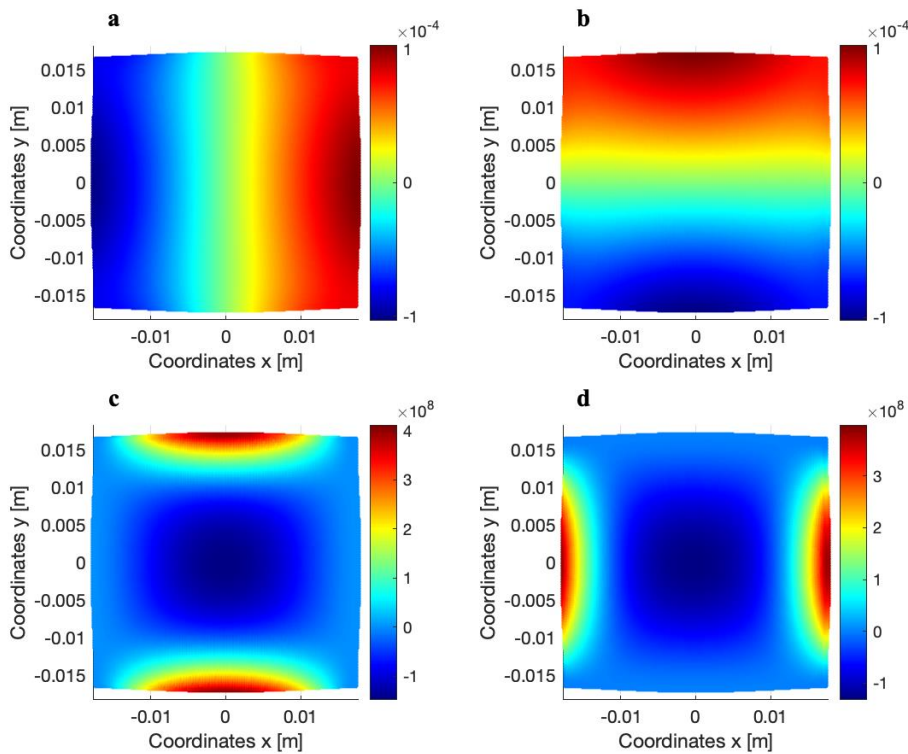


Fig. 8 Displacements in **a** x-direction u [m] and **b** y-direction v [m], Residual stresses **c** σ_x^{rs} [Pa] and **d** σ_y^{rs} [Pa] of the plate with a crack length of $a = 0$ under temperature distribution of $T_{\max} = 1000 \text{ K}$

The calculated residual stresses by means of FEA at the centre line of the sample in Fig. 7 indicating the high tensile stress concentrations near the crack tip with higher longitudinal residual stresses σ_x^{rs} for the higher $T_{\max} > 0$. The sample without the crack with $a = 0$ is in a compression state, but as the crack is initiated in the sample, high tension stress area develops at the crack tip. Similar changes from compressive to tensile residual stresses were noticed

during the pre-notch machining process of the C(T) sample preparation, as discussed by Syed et al. [14]. Moreover, the distribution of the transverse residual stresses σ_y^{rs} in Fig. 7 is very close to the residual stress distributions in [14,20], where the sample without pre-notch is under tensile residual stresses at the areas close to the edges. On the other hand, with the initiation of the notch, the maximum tensile stresses for $T_{\max} > 0$ are in front of the notch tip, followed by compressive stresses.

In Fig. 8c,d, the compressive residual stresses in the plate without a crack are due to the applied parabolic temperature profile where the peak temperatures are in the middle of the plate and the gradual decrease of the temperatures are closer to the plate edges. Compressive stresses happen due to the non-uniform heating and cooling of the plate, where the plate tends to expand due to the heat at the centre, as shown in Fig. 8a,b, but cooling constraining boundaries at the edges are restraining the expansion. On the other hand, when the crack is initiated in the plate, peak residual stresses in Fig. 7 are noticed at the crack tip due to the thermal expansion of the plate when $T_{\max} > 0$ as shown in Fig. 9, followed by the compressive stresses closer to the plate edge with the cooling temperatures. Instead, when $T_{\max} < 0$ the crack closure takes place (Fig. 10a,b) with high compressive stresses at the crack tip (Fig. 10c,d). The increased difference between the heating and the cooling temperatures (parabolic profile) in the plate is resulting in the higher stresses in front of the crack tip, as shown in Fig. 7. The non-uniform temperature distribution in the plate resulting in a subsequent expansion and contraction is the cause of the non-uniform stresses with the peak stress concentrations at the crack tip.

The thermally deformed pre-cracked structure in Fig. 7 will be used for fatigue crack propagation analysis and the stresses at the crack tip will be referred to as maximum residual stress in the sample. With this respect, four models are identified with initial maximum residual stresses of $\sigma_x^{rs} = -203.3, 203.3, 406.6$ and 813.2 MPa , under temperature distributions of $T_{\max} = -250, 250, 500$ and 1000 K , respectively.

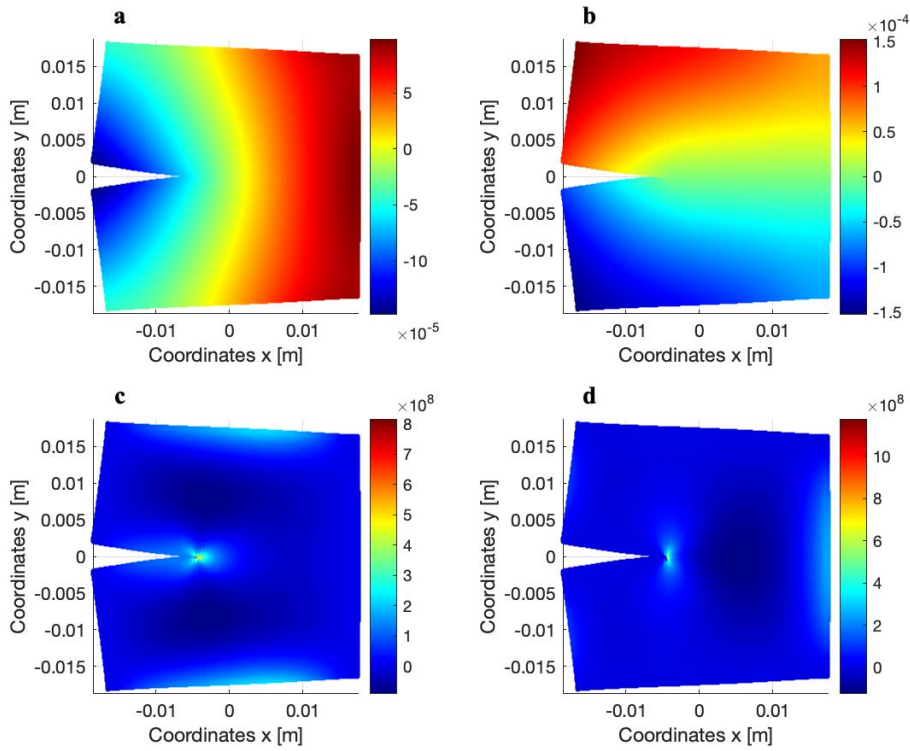


Fig. 9 Displacements in **a** x-direction u [m] and **b** y-direction v [m], Residual stresses **c** σ_x^{rs} [Pa] and **d** σ_y^{rs} [Pa] of the plate with a crack length of $a = 12.4$ mm under temperature distribution of $T_{\max} = 1000$ K

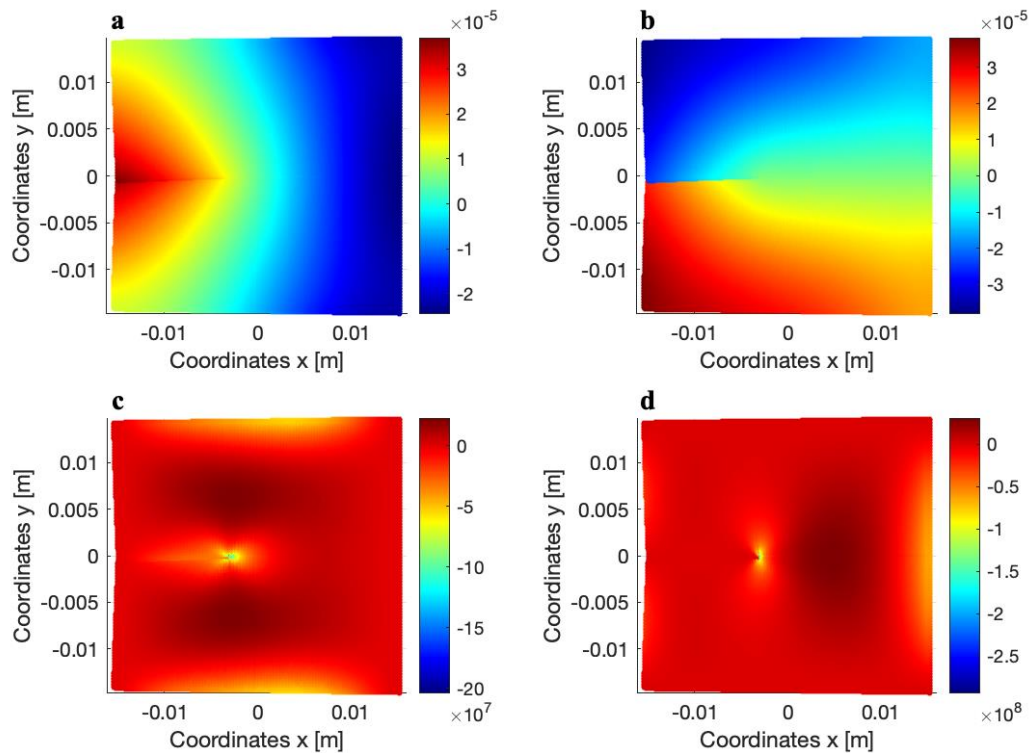


Fig. 10 Displacements in **a** x-direction u [m] and **b** y-direction v [m], Residual stresses **c** σ_x^{rs} [Pa] and **d** σ_y^{rs} [Pa] of the plate with a crack length of $a = 12.4$ mm under temperature distribution of $T_{\max} = -250$ K

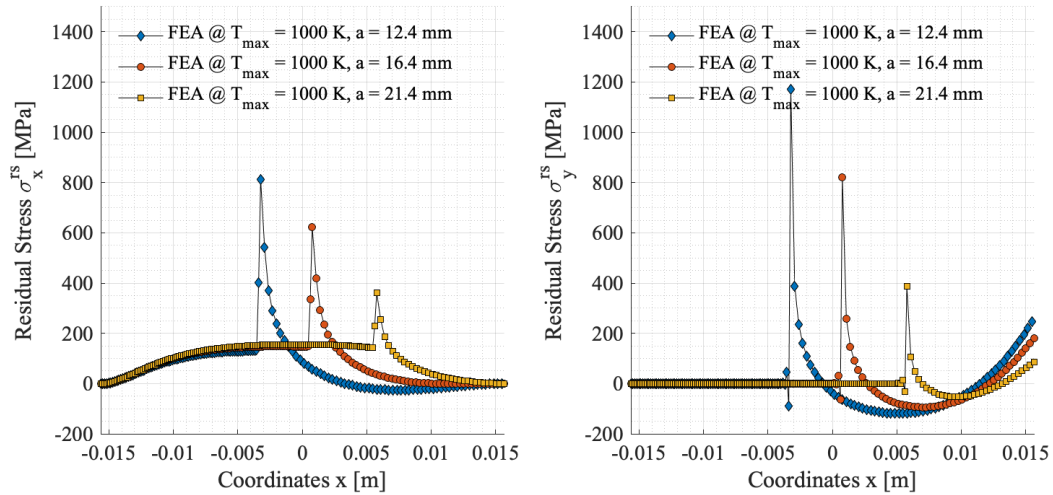


Fig. 11 Residual stresses at the crack tip in the C(T) sample along the centre line $y = 0$ for an increasing crack length of a .

Fig. 11 presents calculated residual stresses by means of FEA versus the crack length along the crack propagation line in the plate under temperature distribution of $T_{\max} = 1000 \text{ K}$. The tensile stress area can be noticed near the crack tip for both longitudinal and transverse directions, at the crack length of $a = 12.4, 16.4$ and 21.4 mm , with the release of residual stresses as the crack propagates.

It can be noted in Fig. 11 that the residual stresses are decreasing with the increased crack length in a plate under the applied parabolic temperature distribution shown in Fig. 6. The following outcome is contrary to the increasing stresses in the plate as the crack propagates due to the tension loading conditions. The decrease in the residual stresses occurs due to the applied temperature profile, as shown in Fig. 11. The cooling temperatures at the edges of the plate result in high residual stresses at the crack tip and compressive residual stresses ahead of the crack. As crack length is increasing, the applied temperatures ahead of the crack tip are lower, compared to the initial crack length of $a = 12.4 \text{ mm}$ and the residual stresses are decreasing. The application of different temperature profiles is resulting in different outcome of residual stresses. For example, the temperature profile in Fig. 13a results in lower residual stresses in Fig. 13b,c than applied parabolic distribution in Fig. 11. The temperature distribution in Fig. 6 with the resulting residual stresses in Fig. 11 is the first iteration of the simplified implementation of initial residual stresses in the AM structure, where the stresses within the

sample are not constant and decreasing as the crack propagates. Multiple variations of the temperature distributions, which could represent the initial residual stresses in the AM samples due to the layer by layer process, are in the interest of further studies.

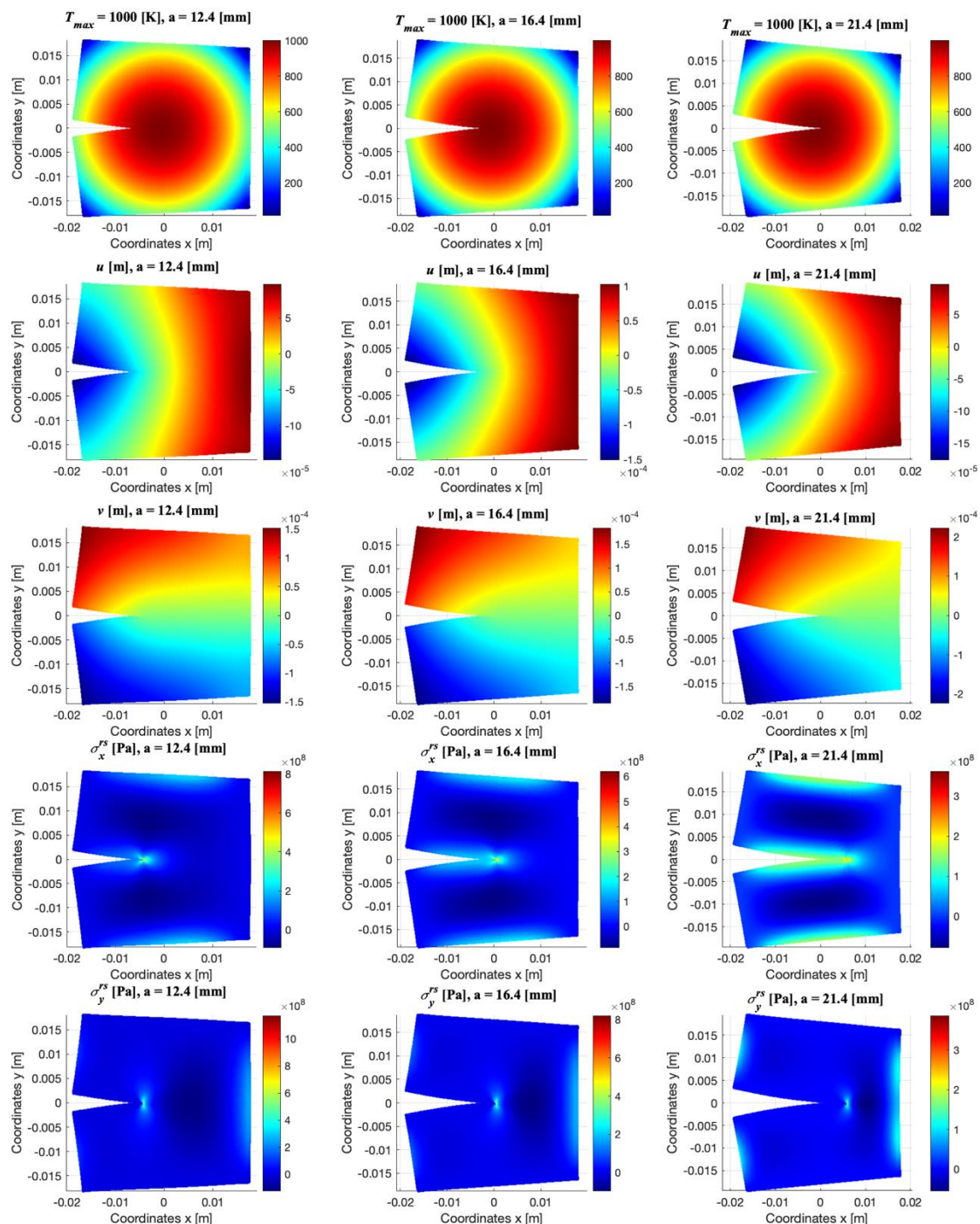


Fig. 12 Temperature distribution, displacements in x-direction (u) and y-direction (v), residual stresses σ_x^{rs} and σ_y^{rs} of the plate with a crack length of $a = 12.4, 16.4$ and 21.4 mm

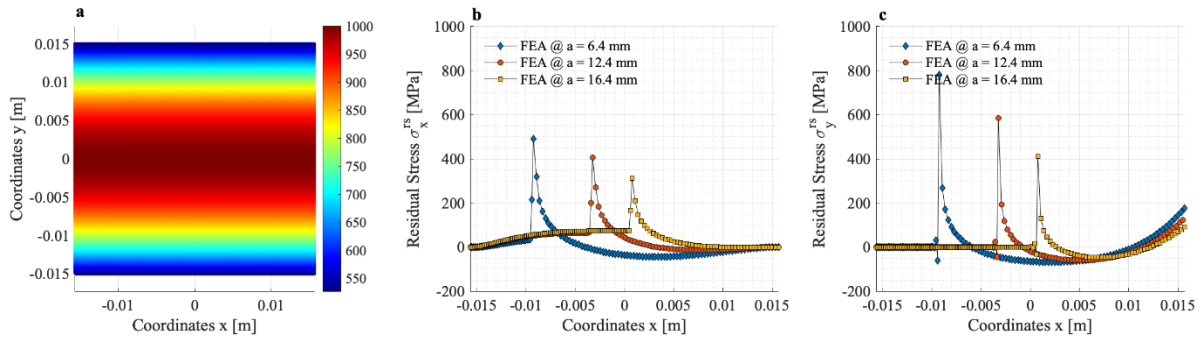


Fig. 13 **a** Temperature distribution, residual stresses **b** σ_x^{rs} and **c** σ_y^{rs} of the plate with a crack length of $a = 6.4, 12.4$ and 16.4 mm

4.2 PD model verification with FEA

The FCG analysis is performed by means of PD and the model is verified with FEA so that the implemented temperature profiles described in Section 4.1 will result in the same residual stress distributions. The PD fatigue model is described in Section 2 and the flowchart of the tension-tension loads and temperature distribution implementation in the PD FCG model is shown in Fig. 14. The parameters and material properties of the titanium alloy Ti6Al4V C(T) sample are specified in Section 3. The thermal expansion coefficient is $\alpha = 8.78 \times 10^{-6}$ 1/K.

Both FEA and PD models are simulated under the parabolic temperature distribution with $T_{\max} = 1000$ K (Fig. 6) as shown in Fig. 15 the PD results are in good agreement with FEA results for the displacements along the centre lines of the plate.

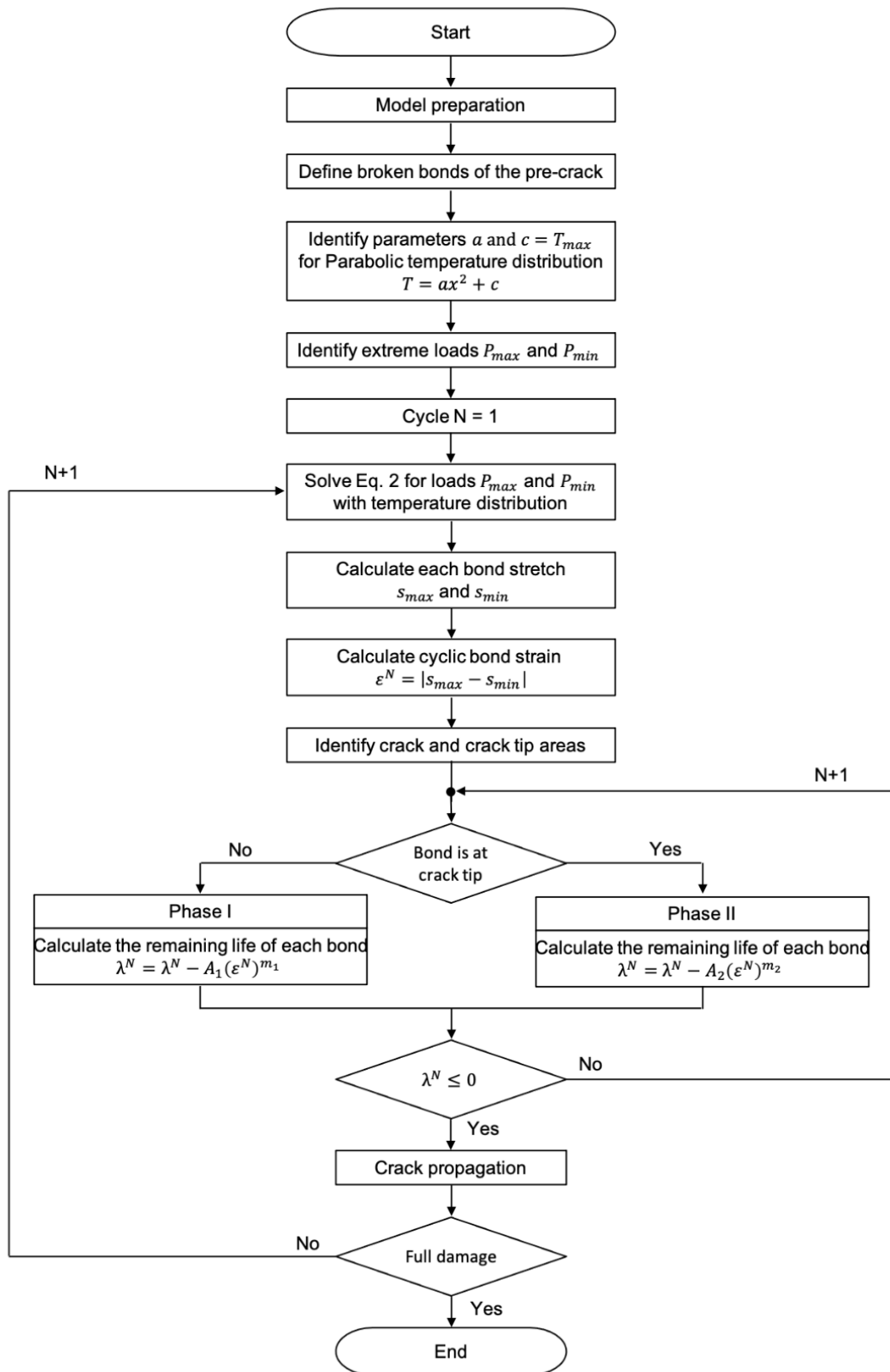


Fig. 14 Flowchart of PD fatigue model with initiated tension-tension loads of P_{max} and P_{min} and temperature distribution with T_{max} .

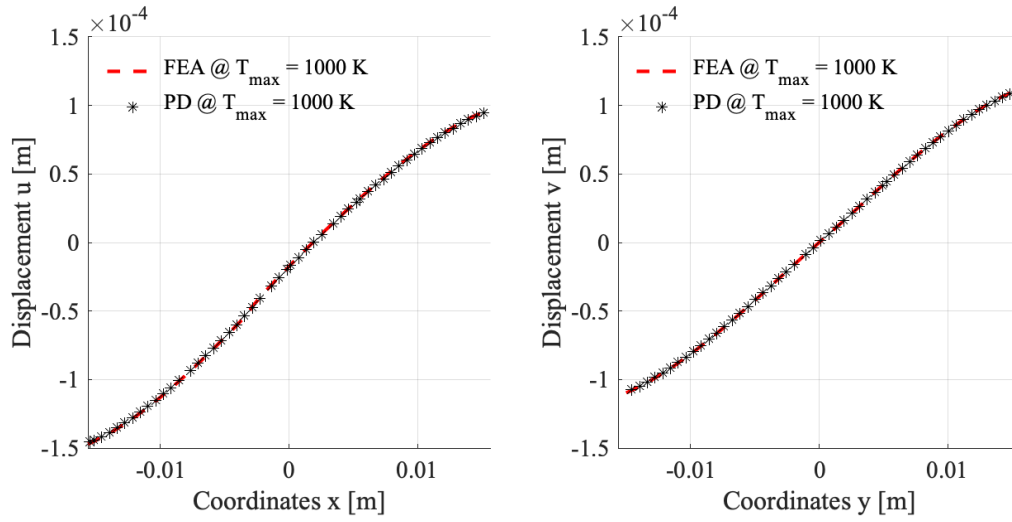


Fig. 15 Displacement variations along the centre lines in a plate with a crack length of $a = 0$

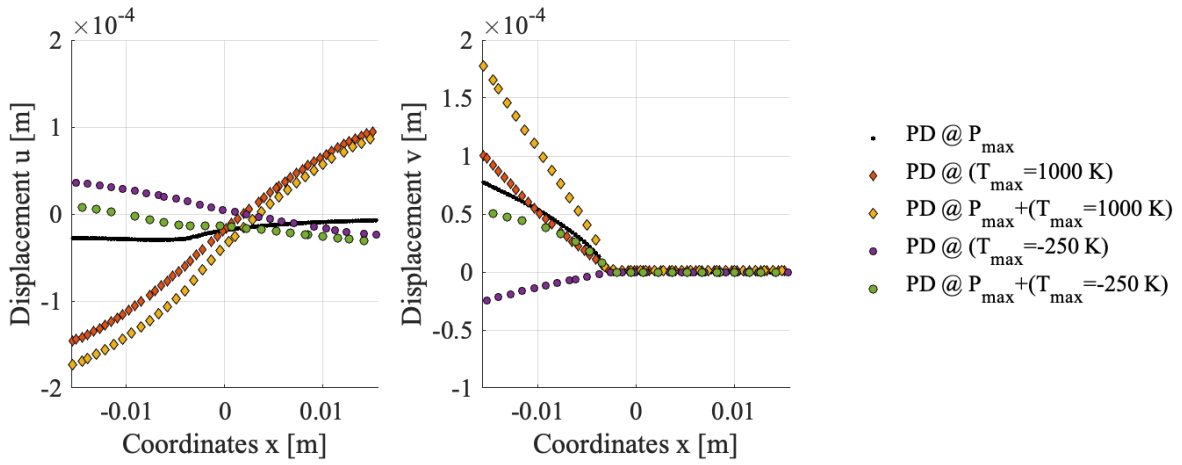


Fig. 16 Comparison between PD predictions of the displacement variations along the centre line $y = 1.5 \times 10^{-4}$ at: tension load $P_{max} = 7 \text{ kN}$ only, temperature distribution with T_{max} only, and combined $P_{max} + T_{max}$.

Utilising PD for the fatigue simulations, the temperature distribution with T_{max} is initiated at each cycle to represent residual stresses in the sample, as shown in Fig. 14. This means that at each cycle of tension-tension with the load ratio of $R = 0.1$ and with the load amplitude of ΔP , the parabolic temperature is introduced. Fig. 16 shows PD models, where only maximum tension load of $P_{max} = 7 \text{ kN}$ is applied at the cut outs (Fig. 4), only temperature distribution with T_{max} is introduced and the combined model with both $P_{max} + T_{max}$. When the tension load of P_{max} occurs together with T_{max} , the displacements are superimposed. In this respect, in Fig. 16, the application of the tension load together with the temperature of $T_{max} = 1000 \text{ K}$, higher displacements are noticeable in the thermally deformed structure under tension loading. The application of temperatures of $T_{max} > 0$ leads to the sample expansion, shown in Fig. 16,

and crack opening. Instead, when the temperatures are $T_{\max} < 0$, the crack closure occurs and under the combined loads of $P_{\max} + (T_{\max} = -250 \text{ K})$, the sum of the displacements is lower compared to the condition with P_{\max} only.

It should be noted that PD FCG simulations for the samples without initial residual stresses (wrought Ti6Al4V in Section 3) is solved by PD equations of motion and the crack propagation is controlled by fatigue damage model described in Section 2. In this way, the stresses in the plate are occurring due to the externally applied loading, which affects crack tip stress fields. Instead, the experimental checks of AM samples [6–8] showed the residual stresses in the material before the crack initiation and propagation processes. With this respect, to initiate the initial residual stresses in the plate due to AM process, the authors proposed to apply parabolic temperature distribution, which results in tensile or compressive stresses in front of the crack tip before the tensile load is applied. It is a simplified method of initiation of pre-tension or pre-compression of the model with the representation of residual stresses. As shown in Fig. 16, the applied loading occurred together with residual stresses (due to the applied temperature distribution), which favours crack opening and promotes the crack propagation, discussed in the next Section 4.3. The current numerical model assumes that the material is linearly elastic, and the effects of the residual stresses due to the temperature distribution and the applied stresses due to the tension loading are superimposed. The following assumption is not an absolutely accurate criterion as the existence of the residual stresses effects on the crack tip stress field and when the sample is loaded, the distribution of plastic strain in the crack tip field occurs [30]. The non-uniform distribution of the residual stresses in the AM structures [6–8] and the internally self-equilibrating stresses due to the crack initiation complicates the prediction of FCGR. It is beneficial for future works to check other temperature profiles for the implementation of initial stresses in the samples due to AM. Still, additional tests and data should be available on initial residual stresses, redistribution of residual stresses due to crack propagation and the effect of the residual stresses on FCGR. Nevertheless, the proposed PD combining residual stresses and applied loading shows promising results in Section 4.3.

4.3 PD fatigue model results and discussions

The PD fatigue model from Section 3 is selected for the study of the FCG in the C(T) sample. The geometry, material properties of the C(T) sample and PD parameters are kept the same. The cyclic load of $\Delta P = 3.15 \text{ kN}$ with the load ratio of $R = 0.1$ is selected.

The simplified model of residual stresses implementation includes the temperature distribution profile from Fig. 6 for each cycle load of ΔP . The following approach of modelling initiates high tensile residual stresses at the crack tip in the plate, as described in Section 4.1. The sample is analysed under three tensile and one compressive residual stresses. The load cases and the resulting stresses at the crack tip are summarised in Table 1.

The PD FCG model is using the Paris' law described in Section 2 where cyclic bond strain ε is proportional to the cyclic SIF and the life of the bonds evolves according to Eq. (5). The applied Paris–Erdogan equation does not explicitly include the crack closure phenomena as it is done by Elber [31,32], which is defining an effective stress intensity range when partial crack closure occurs after unloading the sample. In the current study, the tension-tension loads are applied with the load ratio of $R = 0.1$ and the model is treated as elastic where the phenomena of plasticity-induced crack closure is neglected.

Table 1 Load cases and residual stresses at a crack length of $a = 12.4 \times 10^{-3} \text{ m}$

Type	Parabolic temperature distribution with T_{\max}, K	Residual stresses due to temperature T_{\max} ,		Cyclic load, $\Delta P, kN$
		σ_x^{rs}, MPa	σ_y^{rs}, MPa	
1	1000	813.2	1173	3.15
2	500	406.6	586.3	
3	250	203.3	293.1	
4	-250	-203.3	-293.1	

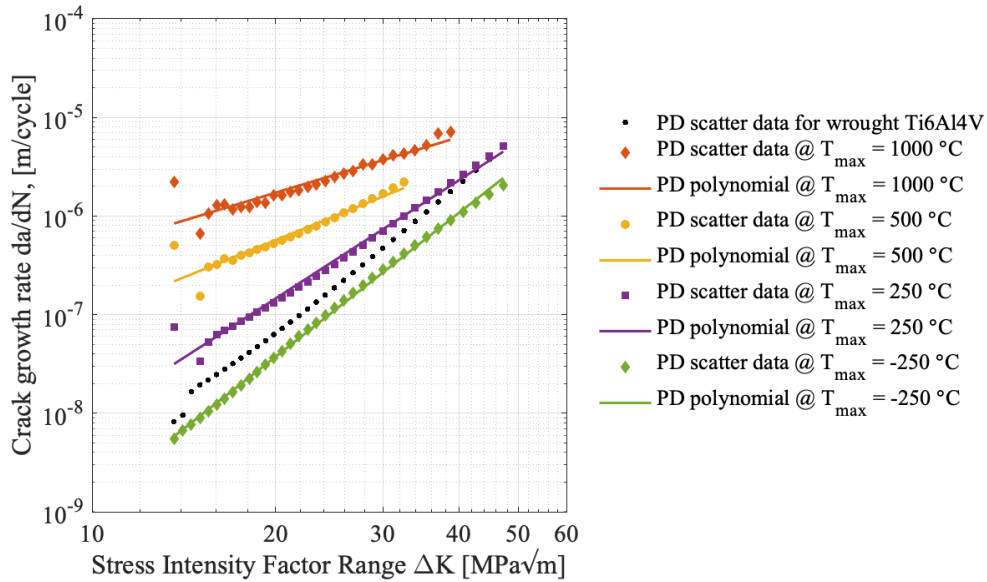


Fig. 17 Crack growth curves comparison for C(T) samples under different temperature distributions.

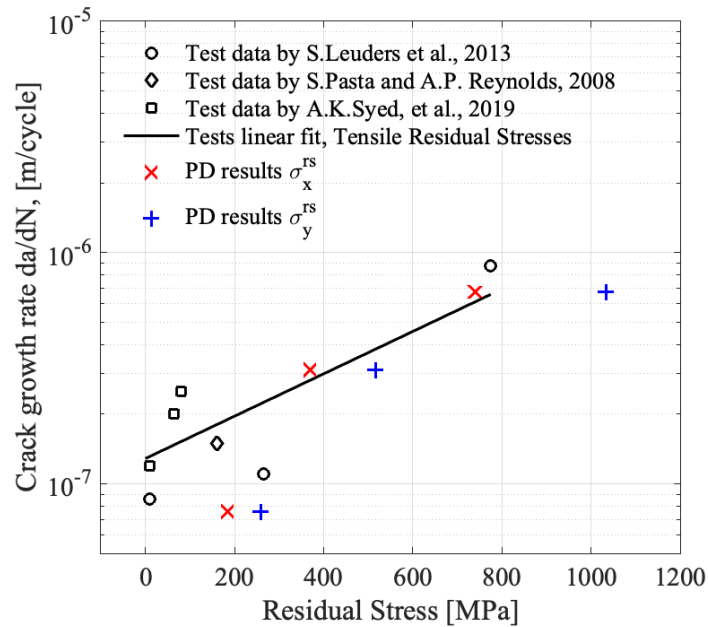


Fig. 18 Fatigue crack growth rates as a function of maximum residual stresses. PD results vs experimental data [8,14,33]

The PD numerical results in Fig. 17 show a great impact of residual stresses on fatigue crack growth rates. The models with high tensile residual stresses cause higher stress concentrations near the crack tip, resulting in a greater FCGR, compared to the wrought Ti6Al4V. This means that the tensile residual stresses in front of the propagating crack add to the tensile loading resulting in faster fracture. Moreover, the existence of the compressive stresses in x and y directions are enhancing the fracture resistance. The compressive stresses are acting to close the crack and reducing the tensile load so that the FCGR is the lowest. The

studies of the additively manufactured Ti6Al4V C(T) samples show that the crack growth is faster in the presence of high tensile residual stresses.

Fig. 18 shows the data obtained from the crack growth rate curves at SIF range of $\Delta K = 16 \text{ MPa}\sqrt{\text{m}}$, reported in the literature [8], where the tests are performed at a load ratio of $R = 0.1$, and the maximum tensile residual stress values are estimated from the reported stress distributions. The PD results in Fig. 18 are presented when the SIF range is $\Delta K = 16 \text{ MPa}\sqrt{\text{m}}$ and the longitudinal $\sigma_x^{rs}, \text{ MPa}$ and the transverse $\sigma_y^{rs}, \text{ MPa}$ residual stresses are evaluated by performing the FEA described in Section 4.1. The SIF of $\Delta K = 16 \text{ MPa}\sqrt{\text{m}}$ has occurred when the crack propagated and the length of the crack is $a = 14 \text{ mm}$. The combined results of PD fatigue model and residual stress evaluations from FEA are presented in Fig. 18. The PD numerical results predicted the FCGR close to the experimental data [8,14,33]. The PD FCGR in the samples with lower residual stresses shows slower crack propagation compared to the tests data. One of the reasons could be microstructure and the process-induced porosities of the samples [8], which are not included in the current study, as well as the simplifications applied in the PD numerical model. On the other hand, the simplified numerical PD model of initiating the residual stresses in the C(T) samples by introducing the temperature profiles in each of the fatigue cycles is capable of predicting the FCGR behaviour and the influence of stresses on the fatigue performance. For example, the study by Leuders et al. [8] reported very high tensile internal stresses of 775 MPa in the built direction and 265 MPa in the scanning direction. The PD results with the stresses in the C(T) sample are close to the experimental studies, and FCGR show quite close results to the test data in Fig. 18.

Both of the tests [8,14,33] and the PD simulations show the dependency of the fatigue performance on the residual stresses with faster crack propagation in the presence of the higher residual stresses. It is clear that the existence of the residual stresses and different levels of residual stresses developed in the AM SLM process are major factors in the anisotropic fatigue behaviour of the samples.

5 Conclusion

In this study, the authors present the numerical approach of modelling the residual stresses in the C(T) samples by means of PD to predict the fatigue response of the additively manufactured Ti6Al4V samples. As layer by layer manufacturing resulting in material anisotropy with the most probable cause of residual stresses existence, the authors looked at the effect of the thermal residual deformations in the fatigue crack propagation. The implementation of the parabolic temperature profile resulted in high residual stresses in front of the crack tip leading to the pre-tension or pre-compression of the sample. The thermal deformations of the plate in the PD model are verified with FEA. A good agreement is found between the PD and FEA simulations, and the model is used for further fatigue analysis. The PD fatigue model with the initial residual stresses shows good predictability of the FCGR, which is consistent with the experimental data available in the literature. The C(T) samples with the high tensile residual stresses have very high-stress concentrations in front of the crack tip, leading to fast crack propagation. On the other hand, compressive residual stresses have a contrary effect on FCGR with lower fracture levels because of the pre-compression of the sample, which is acting to close the crack. The proposed approach of residual stresses implementation in the PD fatigue model showed its capability to capture fatigue damage evolution and applicability on predictions of FCGR of additively manufactured Ti6Al4V samples.

References

- [1] Zhai Y, Lados DA, Lagoy JL. Additive Manufacturing: Making imagination the major Limitation. *Jom* 2014;66:808–16. <https://doi.org/10.1007/s11837-014-0886-2>.
- [2] DebRoy T, Wei HL, Zuback JS, Mukherjee T, Elmer JW, Milewski JO, et al. Additive manufacturing of metallic components – Process, structure and properties. *Prog Mater Sci* 2018;92:112–224. <https://doi.org/10.1016/j.pmatsci.2017.10.001>.
- [3] Bourell D, Kruth JP, Leu M, Levy G, Rosen D, Beese AM, et al. Materials for additive manufacturing. *CIRP Ann - Manuf Technol* 2017;66:659–81. <https://doi.org/10.1016/j.cirp.2017.05.009>.

- [4] Kruth J-P, Leu MC, Nakagawa T. Progress in Additive Manufacturing and Rapid Prototyping. *CIRP Ann* 1998;47:525–40. [https://doi.org/10.1016/s0007-8506\(07\)63240-5](https://doi.org/10.1016/s0007-8506(07)63240-5).
- [5] Xie Y, Gao M, Wang F, Zhang C, Hao K, Wang H, et al. Anisotropy of fatigue crack growth in wire arc additive manufactured Ti-6Al-4V. *Mater Sci Eng A* 2018;709:265–9. <https://doi.org/10.1016/j.msea.2017.10.064>.
- [6] Seifi M, Salem A, Satko D, Shaffer J, Lewandowski JJ. Defect distribution and microstructure heterogeneity effects on fracture resistance and fatigue behavior of EBM Ti–6Al–4V. *Int J Fatigue* 2017;94:263–87. <https://doi.org/10.1016/j.ijfatigue.2016.06.001>.
- [7] Kok Y, Tan XP, Wang P, Nai MLS, Loh NH, Liu E, et al. Anisotropy and heterogeneity of microstructure and mechanical properties in metal additive manufacturing: A critical review. *Mater Des* 2018;139:565–86. <https://doi.org/10.1016/j.matdes.2017.11.021>.
- [8] Leuders S, Thöne M, Riemer A, Niendorf T, Tröster T, Richard HA, et al. On the mechanical behaviour of titanium alloy TiAl6V4 manufactured by selective laser melting: Fatigue resistance and crack growth performance. *Int J Fatigue* 2013;48:300–7. <https://doi.org/10.1016/j.ijfatigue.2012.11.011>.
- [9] Greitemeier D, Palm F, Syassen F, Melz T. Fatigue performance of additive manufactured TiAl6V4 using electron and laser beam melting. *Int J Fatigue* 2017;94:211–7. <https://doi.org/10.1016/j.ijfatigue.2016.05.001>.
- [10] Spierings AB, Starr TL, Wegener K. Fatigue performance of additive manufactured metallic parts. *Rapid Prototyp J* 2013;19:88–94. <https://doi.org/10.1108/13552541311302932>.
- [11] Thijs L, Verhaeghe F, Craeghs T, Humbeeck J Van, Kruth JP. A study of the microstructural evolution during selective laser melting of Ti-6Al-4V. *Acta Mater* 2010;58:3303–12. <https://doi.org/10.1016/j.actamat.2010.02.004>.
- [12] Vrancken B, Cain V, Knutsen R, Van Humbeeck J. Residual stress via the contour method in compact tension specimens produced via selective laser melting. *Scr Mater* 2014;87:29–32. <https://doi.org/10.1016/j.scriptamat.2014.05.016>.
- [13] Rangaswamy P, Griffith ML, Prime MB, Holden TM, Rogge RB, Edwards JM, et al. Residual stresses in LENS® components using neutron diffraction and contour method. *Mater Sci Eng A* 2005;399:72–83. <https://doi.org/10.1016/j.msea.2005.02.019>.
- [14] Syed AK, Ahmad B, Guo H, Machry T, Eatock D, Meyer J, et al. An experimental study of residual stress and direction-dependence of fatigue crack growth behaviour in as-built and stress-relieved selective-laser-melted Ti6Al4V. *Mater Sci Eng A* 2019;755:246–57. <https://doi.org/10.1016/j.msea.2019.04.023>.
- [15] Mughal MP, Fawad H, Mufti RA, Siddique M. Deformation modelling in layered manufacturing of

- metallic parts using gas metal arc welding: Effect of process parameters. *Model Simul Mater Sci Eng* 2005;13:1187–204. <https://doi.org/10.1088/0965-0393/13/7/013>.
- [16] Alimardani M, Toyserkani E, Huissoon JP. A 3D dynamic numerical approach for temperature and thermal stress distributions in multilayer laser solid freeform fabrication process. *Opt Lasers Eng* 2007;45:1115–30. <https://doi.org/10.1016/j.optlaseng.2007.06.010>.
- [17] Mukherjee T, Zhang W, DebRoy T. An improved prediction of residual stresses and distortion in additive manufacturing. *Comput Mater Sci* 2017;126:360–72. <https://doi.org/10.1016/j.commatsci.2016.10.003>.
- [18] Parry L, Ashcroft IA, Wildman RD. Understanding the effect of laser scan strategy on residual stress in selective laser melting through thermo-mechanical simulation. *Addit Manuf* 2016;12:1–15. <https://doi.org/10.1016/j.addma.2016.05.014>.
- [19] ASTM E647–13. Standard Test Method for Measurement of Fatigue Crack Growth Rates. *Am Soc Test Mater* 2014;03:1–50. <https://doi.org/10.1520/E0647-13A.2>.
- [20] Mercelis P, Kruth JP. Residual stresses in selective laser sintering and selective laser melting. *Rapid Prototyp J* 2006;12:254–65. <https://doi.org/10.1108/13552540610707013>.
- [21] Wang Z, Denlinger E, Michaleris P, Stoica AD, Ma D, Beese AM. Residual stress mapping in Inconel 625 fabricated through additive manufacturing: Method for neutron diffraction measurements to validate thermomechanical model predictions. *Mater Des* 2017;113:169–77. <https://doi.org/10.1016/j.matdes.2016.10.003>.
- [22] Silling SA. Reformulation of elasticity theory for discontinuities and long-range forces. *J Mech Phys Solids* 2000;48:175–209. [https://doi.org/10.1016/S0022-5096\(99\)00029-0](https://doi.org/10.1016/S0022-5096(99)00029-0).
- [23] Silling S, Askari A. Peridynamic model for fatigue cracks. 2014.
- [24] Karpenko O, Oterkus S, Oterkus E. Peridynamic Investigation of the Effect of Porosity on Fatigue Nucleation for Additively Manufactured Titanium Alloy Ti6Al4V. *Theor Appl Fract Mech* 2021;102925. <https://doi.org/10.1016/j.tafmec.2021.102925>.
- [25] Silling SA, Askari E. A meshfree method based on the peridynamic model of solid mechanics. *Comput Struct* 2005;83:1526–35. <https://doi.org/10.1016/j.compstruc.2004.11.026>.
- [26] Madenci E, Oterkus E. *Peridynamic Theory and Its Applications*. Springer New York Heidelberg Dordrecht London; 2014. [https://doi.org/DOI 10.1007/978-1-4614-8465-3](https://doi.org/DOI%2010.1007/978-1-4614-8465-3).
- [27] Silling SA, Bobaru F. Peridynamic modeling of membranes and fibers. *Int J Non Linear Mech* 2005;40:395–409. <https://doi.org/10.1016/j.ijnonlinmec.2004.08.004>.
- [28] Liu X, Sun C, Hong Y. Effects of stress ratio on high-cycle and very-high-cycle fatigue behavior of a Ti-6Al-4V alloy. *Mater Sci Eng A* 2015;622:228–35. <https://doi.org/10.1016/j.msea.2014.09.115>.

- [29] Van Hooreweder B, Moens D, Boonen R, Kruth JP, Sas P. Analysis of fracture toughness and crack propagation of Ti6Al4V produced by selective laser melting. *Adv Eng Mater* 2012;14:92–7. <https://doi.org/10.1002/adem.201100233>.
- [30] Coules HE, Smith DJ, Orrock PJ, Abburi Venkata K, Pirling T. A Combined Experimental and Modelling Approach to Elastic–Plastic Crack Driving Force Calculation in the Presence of Residual Stresses. *Exp Mech* 2016;56:1313–25. <https://doi.org/10.1007/s11340-016-0171-0>.
- [31] ELBER W. Fatigue Crack Closure Under Cyclic Tension. *Eng Fract Mech* 1970;2:37–44. [https://doi.org/10.1016/0013-7944\(70\)90028-7](https://doi.org/10.1016/0013-7944(70)90028-7).
- [32] ELBER W. the Significance of Fatigue Crack Closure. *ASTM Spec Tech Publ* 1971:230–42.
- [33] Pasta S, Reynolds AP. Residual stress effects on fatigue crack growth in a Ti-6Al-4V friction stir weld. *Fatigue Fract Eng Mater Struct* 2008;31:569–80. <https://doi.org/10.1111/j.1460-2695.2008.01258.x>.